

Extended optical model analyses of $^{11}\text{Be}+^{197}\text{Au}$ with dynamic polarization potentials

Kyoungsu Heo and Myung-Ki Cheoun*

*Department of Physics and Origin of Matter and Evolution of Galaxy (OMEG) Institute,
Soongsil University, Seoul 06978, Korea*

Ki-Seok Choi and K. S. Kim

School of Liberal Arts and Science, Korea Aerospace University, Koyang 10540, Korea

W. Y. So

*Department of Radiological Science, Kangwon
National University at Dogye, Samcheok 25945, Korea*

(Dated: November 26, 2018)

We discuss angular distributions of elastic, inelastic, and breakup cross sections for $^{11}\text{Be} + ^{197}\text{Au}$ system, which were measured at energies below and around Coulomb barrier. To this end, we employ Coulomb dipole excitation (CDE) and long-range nuclear (LRN) potential to take into account long range effects by halo nuclear system and break up effects by weakly-bound structure. We then analyze recent experimental data including 3-channels *i.e.* elastic, inelastic, and breakup cross sections, at $E_{\text{c.m.}}=29.6$ MeV and $E_{\text{c.m.}}=37.1$ MeV. From the extracted parameter sets using χ^2 analysis, we successfully reproduce the experimental angular distributions of the elastic, inelastic, and breakup cross sections for $^{11}\text{Be}+^{197}\text{Au}$ system simultaneously. Also we discuss the necessity of LRN potential around Coulomb barrier from analyzed experimental data.

* e-mail: cheoun@ssu.ac.kr

I. INTRODUCTION

Optical model (OM) is a traditional analysis tool for elastic scattering from the beginning of nuclear physics. It provides valuable information of the nuclear interactions between projectile and target nucleus in the nuclear reaction. Especially, it is of benefit to understand the elastic scattering and other direct reactions simultaneously by using χ^2 analysis. In practise, the parameters extracted from OM analysis are useful for other microscopic approaches such as distorted wave born approximation (DWBA) or continuum-discretized coupled-channels (CDCC) for treating contributions of inelastic and transfer channels. Actually, elastic channel itself encompasses all participating direct reaction channel information, such as, inelastic, breakup, etc [1]. Lots of efforts to separate each channel contribution from the elastic scattering cross section have been continued. For example, it is well known that the dynamic polarization potential (DPP) [2] related with E2 transition is useful for taking into account the contribution of inelastic channels in elastic scattering. If we know all potentials corresponding to each nuclear reaction channel, we could simultaneously calculate cross sections of by each nuclear reaction channel with a proper parameter set.

We have been extending the OM analysis by including DPP which comprises potentials from breakup and fusion reaction channel [3, 4]. Especially, the nuclear reactions including halo nuclei have been analyzed with the OM approach, because those halo nuclei are exhibiting obviously different behavior from known stable nuclei [5–9]. For example, well-known light halo nuclei such as ^{11}Li or ^6He have a specific feature owing to the halo nuclei composed by a charged core and neutral one (two) valence neutron(s). The charged core only responds to the Coulomb interaction by a target nucleus, but the valence neutron(s) does not act to the Coulomb one. Consequently, inelastic and breakup channel are opened on this weakly-bound structure. These phenomena by Coulomb interaction are called as Coulomb dipole excitation (CDE) [10–12]. The Coulomb breakup channels are such examples from these phenomena. Furthermore, they also show a quite large distance of between the core nucleus and valence neutron(s) termed as a halo structure by the weak binding energy [13].

Recently, interesting experimental researches including light neutron rich nuclei projectile such as $^6,8\text{He}$ [14, 15], ^{11}Li [16–19] and ^{11}Be [20, 21] and so on, have been carried out. More recently, angular distribution data of $^{11}\text{Be}+^{197}\text{Au}$ system including 3-channels *i.e.* elastic, inelastic and breakup cross sections around Coulomb barrier are reported [22]. Therefore,

in this paper, we focus on the nuclear reaction involving ^{11}Be which is a well known halo nucleus constructed with a core nucleus ^{10}Be and one weakly bound valence neutron.

In our preceding paper [8], we already have calculated inelastic scattering for $^{11}\text{Be}+^{197}\text{Au}$ system at $E_{\text{c.m.}}=30.1$ MeV below Coulomb barrier ($V_B \approx 37.9$ MeV) by taking into account the first excitation state, whose results have shown good agreement with experimental data. However, it has only contained inelastic channels without breakup cross section, which are involved in recent experimental data [22]. Therefore, in this paper, we revisit the system and calculate angular distributions of ^{11}Be on ^{197}Au , which were measured at energies below and around Coulomb barrier, $E_{\text{c.m.}}=29.6$ and 37.1 MeV, with elastic, inelastic, and breakup channels. In addition, we try simultaneous description of those elastic, inelastic and breakup cross section data with OM approach by considering long range DPPs such as CDE and long range nuclear (LRN) potential.

The paper is organized as follows. In Sec. 2, we introduce the optical model potential and its formalism implemented in the present work. In Sec. 3, we discuss the simultaneous treatment of elastic, inelastic and breakup cross sections using long range DPPs, such as LRN and CDE potential, with numerical results. Specifically, we discuss the necessity of LRN potential for proper understanding angular distribution data of the reaction relevant to halo nuclei. We finally summarize and conclude our discussions in Sec. 4.

II. FORMALISM

A. Optical model potential

For simultaneous analysis of all participating nuclear reactions in the scattering, the OM Schrödinger equation is expressed as follows [23–26]:

$$[E - T_l(r)]\chi_l^{(+)}(r) = U_{\text{OM}}(r) \chi_l^{(+)}(r), \quad (1)$$

where $T_l(r)$ is a kinetic energy operator and $\chi_l^{(+)}(r)$ is a distorted partial wave function, respectively. The kinetic operator is a function of the angular momentum l ,

$$T_l(r) = -\frac{\hbar^2}{2\mu} \left(\frac{d^2}{dr^2} - \frac{l(l+1)}{r^2} \right), \quad (2)$$

where μ and l are reduced mass and angular momentum, respectively. In the present calculation, the OM potential $U_{\text{OM}}(r)$ comprises the Coulomb potential $U_C(r)$, the nuclear

potential $U_N(r)$, and the CDE potential $U_{\text{CDE}}(r)$ as follows:

$$\begin{aligned}
U_{\text{OM}}(r) &= U_{\text{C}}(r) - U_N(r) - U_{\text{CDE}}(r) \\
&= U_{\text{C}}(r) - [V_N(r) + iW_N(r)] \\
&\quad - [V_{\text{CDE}}(r) + iW_{\text{CDE}}(r)].
\end{aligned}
\tag{3}$$

All participating potentials except Coulomb potential, $U_{\text{C}}(r)$, are consisted of a real part $V(r)$ and an imaginary part $W(r)$. In general, the real part of potential has influence cross sections of elastic scattering, while the imaginary part is in charge of the absorption by each channel in OM approach. Therefore, we assign a different imaginary type to each channel.

B. Nuclear potentials

For halo structure of ^{11}Be , we consider the nuclear potential, $V_N(r)$, in Eq. (3) as coming from two different nuclear interactions, which are between core part of projectile and target nucleus, and between one valence neutron part of projectile and target nucleus, in the scattering of $^{11}\text{Be} + ^{197}\text{Au}$ system.

First, for the interaction between the core nucleus, ^{10}Be , and the target nucleus, ^{197}Au , which interaction is termed as the short-range (bare) nuclear potential (SRN) in this calculation, we employ a complex Woods-Saxon potential in a volume-type form. In order to extract the short-range bare potential parameters for $^{11}\text{Be} + ^{197}\text{Au}$ system, we have to use the experimental elastic scattering data of $^{10}\text{Be} + ^{197}\text{Au}$ system. Unfortunately, however, there are no proper elastic scattering data at and above Coulomb barrier energy. Thus, potential parameters for SRN are deduced from the χ^2 analysis by using the experimental elastic scattering data of $^{10}\text{Be} + ^{208}\text{Pb}$ system [27] and these extracted parameters will be replaced as the bare potential parameters of $^{10}\text{Be} + ^{197}\text{Au}$ system in this work. The parameter set deduced from $^{10}\text{Be} + ^{197}\text{Au}$ system is listed in Table I.

The other interaction is the interaction between one valence neutron of projectile and target nucleus. Strictly speaking, this interaction must also be considered as a part of the short-range bare potential for $^{11}\text{Be} + ^{197}\text{Au}$ system in the OM analysis, if the projectile were stable, or within the three-body system. But, one valence neutron in the projectile ^{11}Be nucleus is easily detached by Coulomb and nuclear interactions generated from target nucleus, and the breakup reaction occurs mainly around the verge of ^{11}Be nucleus during

V_0^{sh}	W_0^{sh}	a_0^{sh}	a_W^{sh}	r_0^{sh}	r_W^{sh}
(MeV)	(MeV)	(fm)	(fm)	(fm)	(fm)
113	169	0.63	0.30	1.06	1.20

TABLE I. The optical model parameters for SRN potential for $^{10}\text{Be} + ^{208}\text{Pb}$ system adopted from Ref. [27]. Here, $r_i = R_i/(A_1^{1/3} + A_2^{1/3})$ with $i = 0$ and W where 0 is real part and W is imaginary part. A_1 and A_2 are masses of projectile and target nuclei, respectively.

the reaction process. Therefore, the interaction between one valence neutron of projectile and target nucleus may give rise to both features from the short-range (bare) potential and the long range DPP associated with the breakup effect occurring at a distance. In this work, however, we do not separate both the short-range bare potential and the long range DDP. Instead, we introduce a new long-range nuclear potential (LRN) with a surface-type Woods-Saxon potential corresponding to the nuclear interaction between one valence neutron of projectile and target nucleus, which is given as follows:

$$U_0^{\text{lo}}(r) = (V_0^{\text{lo}} + iW_0^{\text{lo}})f(X_0^{\text{lo}}), \quad (4)$$

where $f(X_0^{\text{lo}}) = 4a_0^{\text{lo}} \frac{df(X_0^{\text{lo}})}{dR_0^{\text{lo}}}$ with $X_0^{\text{lo}} = (r - R_0^{\text{lo}})/a_0^{\text{lo}}$ and $R_0^{\text{lo}} = r_0^{\text{lo}} (A_1^{1/3} + A_2^{1/3})$. Here the parameter set for LRN potential is determined by χ^2 analysis of both data.

Resultant parameter sets for LRN potential in this calculation are tabulated in Table II, which are determined by the variation of the radius, $r_0^{\text{lo}} = r_W^{\text{lo}}$, from 1.5 to 3.5 fm. To find reasonable parameters, we exploit a simultaneous fitting of the elastic and breakup cross section data and find the optimum values for the four adjustable parameters, that is, V_0^{lo} , W_0^{lo} , $a_0^{\text{lo}} = a_W^{\text{lo}}$. Note that we assume that radius of real part and diffuseness, r_0^{lo} and a_0^{lo} , are the same with r_W^{lo} and a_W^{lo} to reduce number of the parameters. We found that the diffuseness parameter, $a_0^{\text{lo}} = a_W^{\text{lo}}$, is decreased with the increase of the radius.

$E_{c.m.}$ (MeV)	set	V_0^{lo}	W_0^{lo}	$a_0^{lo} = a_W^{lo}$	$r_0^{lo} = r_W^{lo}$	χ^2
(MeV)		(MeV)	(MeV)	(fm)	(fm)	
37.1	(A)	-0.712	0.0085	5.12	1.5	1.41
	(B)	-0.118	0.0016	5.03	2.5	2.41
	(C)	-0.036	0.0010	4.72	3.5	2.53
29.6	(A)	-0.203	0.0094	7.58	1.5	0.73
	(B)	-0.078	0.0044	7.08	2.5	0.82
	(C)	-0.028	0.0022	6.24	3.5	1.03

TABLE II. Parameter sets of LRN potential with a surface-type used in Eq. (4) for $^{11}\text{Be} + ^{197}\text{Au}$ system. Here, $r_i^{lo} = R_i^{lo}/(A_1^{1/3} + A_2^{1/3})$ with $i = 0$ and W .

Here, we shortly summarize the nuclear interaction potential which is divided into two parts, short-range and long-range interaction potential, as follows :

$$\begin{aligned}
U_N(r) &= U_0^{\text{sh}}(r) + U_0^{\text{lo}}(r) \\
&= [V_0^{\text{sh}}(r) + iW_0^{\text{sh}}(r)] \\
&\quad + [V_0^{\text{lo}}(r) + iW_0^{\text{lo}}(r)].
\end{aligned} \tag{5}$$

where subscript "sh" is SRN and "lo" is LRN potential. Also $V(r)$ is a real part and $W(r)$ is an imaginary part, respectively.

C. Coulomb dipole excitation potential

Owing to the weakly bound structure of ^{11}Be , valence neutron in projectile is easily detached from the core ^{10}Be , or projectile is excited due to Coulomb interaction between projectile and target nuclei. These phenomena showed up as strong absorption at forward angle region in the angular distribution of elastic scattering, because Coulomb interaction is long range interaction. Therefore, we have to consider another long range potential by Coulomb interaction.

To take into account the excitation and breakup effects in the long-range region by

Coulomb interaction, we employ CDE potential, U_{CDE} , which is constructed by two parts

$$U_{\text{CDE}} = U_{\text{CDE}}^{\text{inel}} + U_{\text{CDE}}^{\text{br}} = (V_{\text{CDE}}^{\text{inel}} + iW_{\text{CDE}}^{\text{inel}}) + (V_{\text{CDE}}^{\text{br}} + iW_{\text{CDE}}^{\text{br}}), \quad (6)$$

where $U_{\text{CDE}}^{\text{inel}}$ and $U_{\text{CDE}}^{\text{br}}$ are CDE potential for excitation and breakup channel, respectively.

Detailed forms of $U_{\text{CDE}}^{\text{inel}}$ and $U_{\text{CDE}}^{\text{br}}$ are summarized as follows [5–10, 12] :

$$U_{\text{CDE}}^{\text{inel}}(r) = \frac{4\pi Z_t^2 e^2 B(E1; \varepsilon_x^{1st})}{9 \hbar v (r - a_0)^2 r} \times [g(\frac{r}{a_0} - 1, \xi) + if(\frac{r}{a_0} - 1, \xi)] \quad (7)$$

and

$$U_{\text{CDE}}^{\text{br}}(r) = \frac{4\pi Z_t^2 e^2}{9 \hbar v (r - a_0)^2 r} \int_{\varepsilon_b}^{\infty} d\varepsilon \frac{dB(E1)}{d\varepsilon} \times [g(\frac{r}{a_0} - 1, \xi) + if(\frac{r}{a_0} - 1, \xi)] \quad (8)$$

with

$$f(\frac{r}{a_0} - 1, \xi) = 4\xi^2 (\frac{r}{a_0} - 1)^2 \exp(-\pi\xi) K_{2i\xi}''[2\xi(\frac{r}{a_0} - 1)],$$

where a_0 is a distance of the closest approach in head-on collision and Z_t is a charge number of target nucleus. K'' is the second derivative of a modified Bessel function and $\xi = a_0\varepsilon/\hbar v$ is an adiabatic parameter [10].

The expression $g(\frac{r}{a_0} - 1, \xi)$ in Eqs. (7) and (8) is a real part of CDE potential extracted from the dispersion relation [10] given by

$$g(\frac{r}{a_0} - 1, \xi) = \frac{P}{\pi} \int_{-\infty}^{\infty} \frac{f(\frac{r}{a_0} - 1, \xi')}{\xi - \xi'} d\xi'. \quad (9)$$

In Eq. (8), we employ the Coulomb strength distribution $dB(E1)/d\varepsilon$ as a simple model proposed from Ref.[28] as follows:

$$\begin{aligned} \frac{dB(E1)}{d\varepsilon} &= S \frac{\exp(2\kappa r_0)}{1 + \kappa r_0} \frac{3\hbar^2}{\pi^2 \mu} e^2 \left(\frac{Z_1}{A_1}\right)^2 \frac{\sqrt{S_n}(\varepsilon - S_n)^{3/2}}{\varepsilon^4} \\ &= N \frac{\sqrt{S_n}(\varepsilon - S_n)^{3/2}}{\varepsilon^4}, \end{aligned} \quad (10)$$

where S is the spectroscopic factor having 1.0 ± 0.2 value and $\kappa = \sqrt{2\mu S_n}/\hbar$ is a wave number related to neutron separation energy, S_n , respectively. Reduced mass is given as μ , and r_0 is a radius of the nuclear potential with a square-well type related to the halo $^{10}\text{Be} + n$ system.

One can also find some dependencies on S_n as well as a proportional normalization constant N introduced Ref. [6]. In this work, we fix the proportional normalization constant N as 3.1 [6]. All results depend on this normalization constant, but it does change an overall scale, but no shape difference. For S_n , we employ experimental data, 0.501 MeV, in Ref. [28].

D. Angular distribution

To investigate the cross section by each potential discussed above, we use the following form [23]:

$$\frac{d\sigma_i}{d\Omega} = \frac{ka_0}{16\pi} \frac{1}{\cos(\frac{\theta_{c.m.}}{2}) \sin^3(\frac{\theta_{c.m.}}{2})} \sum_l \frac{\pi}{k} (2l+1) T_{i;l}, \quad i = \text{BU and inel} \quad (11)$$

with

$$T_{\text{BU};l} = \frac{8}{\hbar v} \int_0^\infty |\chi_l^+(r)|^2 [W_{\text{CDE}}^{\text{br}}(r) + W^{\text{lo}}(r)] dr \quad (12)$$

for breakup reaction, and

$$T_{\text{inel};l} = \frac{8}{\hbar v} \int_0^\infty |\chi_l^+(r)|^2 [W_{\text{CDE}}^{\text{inel}}(r)] dr \quad (13)$$

for inelastic scattering. Here, k is the wave number defined by $\sqrt{2\mu E_{c.m.}}/\hbar$. The distance of the closest approach, a_0 , in a head-on collision is defined by a classical relation

$$b = \frac{l}{k} = \frac{a_0}{2} \cot\left(\frac{\theta_{c.m.}}{2}\right), \quad (14)$$

where impact parameter b is given as a function of l and $\theta_{c.m.}$. In Eq. (12), we assume that long-range absorption part, W^{lo} , contributes to breakup process, because only one excite states is included in the inelastic process.

III. RESULTS

A. Elastic and quasi-elastic scattering

First, we present results of elastic and quasi-elastic (QE) scattering cross sections using the long range dynamic polarization potentials (DPPs) in Eq. (3). To analyze elastic cross section data, we investigate the ratio of the elastic scattering cross section to Rutherford cross section, $P_E = \sigma_{\text{el}}/\sigma_{\text{RU}}$, in terms of a function of center of mass angle $\theta_{c.m.}$. Figure 1

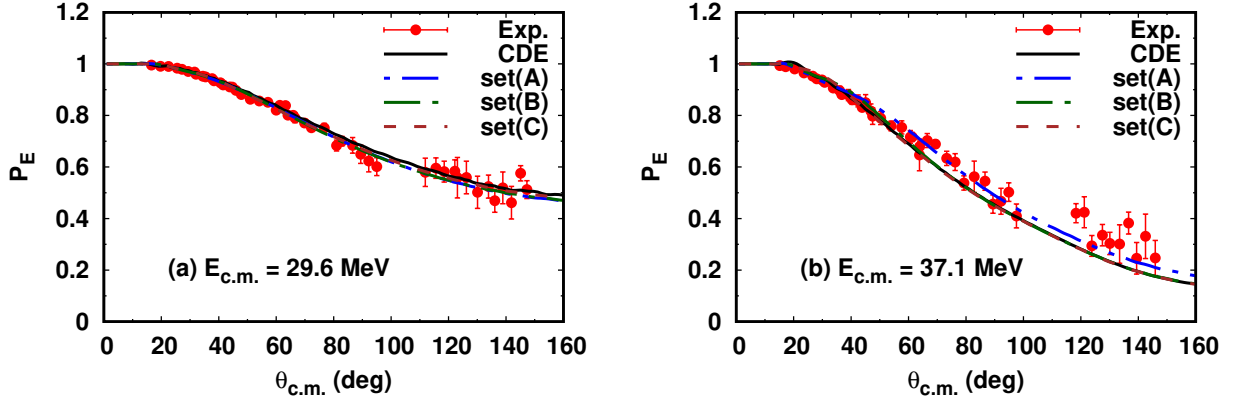


FIG. 1. (Color online) Differential elastic scattering cross section ratio $P_E = \sigma_{el}/\sigma_{RU}$ of $^{11}\text{Be} + ^{197}\text{Au}$ system at $E_{c.m.}=29.6$ MeV(a) and $E_{c.m.}=37.1$ MeV (b). The solid line is the ratio P_E without the LRN potential and the dashed lines (blue, green and brown) are obtained by using the parameter sets in Table II. Red circles are experimental elastic scattering data for $^{11}\text{Be} + ^{197}\text{Au}$ system taken from Ref. [22].

presents the elastic scattering results given by the ratio P_E at two different energies below and around Coulomb barrier, $E_{c.m.}=29.6$ and 37.1 MeV, respectively.

In Fig. 1, the solid line means the ratio P_E without the LRN potential, *i.e.* $U_{OM}(r) = U^{sh}(r) + U_{CDE}(r)$, and the dashed lines (blue, green and brown) mean with the LRN potential, $U_{OM}(r) = U^{sh}(r) + U^{lo}(r) + U_{CDE}(r)$, using the parameters set (A), (B) and (C) in Table II respectively.

In Fig. 1, both results at $E_{c.m.} = 29.6$ MeV and $E_{c.m.} = 37.1$ MeV show good and reasonable agreements with experimental data. In the results at $E_{c.m.} = 29.6$ MeV (Fig. 1(a)), all sets including LRN potential show almost same results albeit different parameter sets. We can easily notice that the LRN contribution shows only a slight difference with the solid line obtained without LRN potential at backward angles. Moreover, the effect of LRN potential at forward angle related to the long range region is shown to be insignificant compared to CDE potential result denoted as the solid black line. Therefore, we could not conclude whether the LRN potential is necessary or not in these ratios for the elastic scattering in Fig. 1(a). In Fig. 1(b) for $E_{c.m.} = 37.1$ MeV, however, we noticed that the ratio P_E obtained by adding LRN potential is significantly suppressed at forward angle ($15^\circ \leq \theta_{c.m.} \leq 40^\circ$) than that by CDE potential, although it is obscure in Fig. 1(b). It can be inferred that

the strong breakup reaction by the LRN potential occurred at forward angle and the elastic scattering was reduced. Thus, this result demonstrates the necessity of LRN potential.

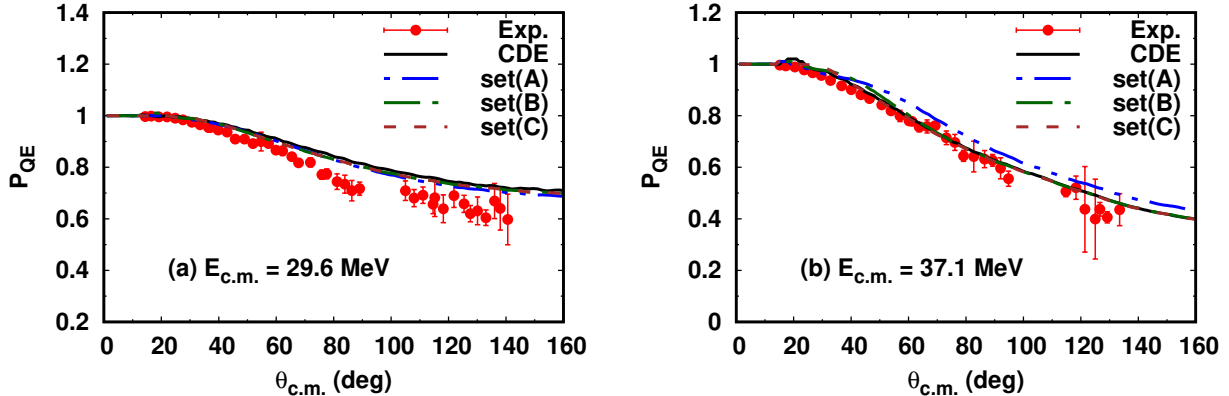


FIG. 2. (Color online) The same as Fig. 1 but for quasi-elastic (QE) scattering cross section. The experimental QE scattering data are taken from Ref. [29].

Figure 2 presents QE scattering results with the same condition as used in elastic scattering in Fig. 1. Here, QE scattering means a sum of elastic scattering and inelastic scattering cross section as defined in Ref. [29].

For this calculation, we estimate inelastic cross section using the inelastic potential part in Eq. (7) and add it to the previous results from the elastic cross section shown in Fig. 1. In next subsection, the inelastic scattering results are compared with the experimental data. From the viewpoint of QE channel, the remaining cross sections, excluding elastic and inelastic ones, will be the cross sections due to the breakup reaction and fusion channels. Since the energy region considered here is below and around Coulomb barrier, however, the contribution of the fusion cross section is not expected to be large at forward angle. It means that the absorption appeared in the forward angle in Fig. 2 almost stems from the breakup contribution by Coulomb and nuclear interactions.

In the results of $E_{c.m.} = 29.6$ MeV(Fig. 2(a)), all results slightly overestimated experimental data. In the case of $E_{c.m.} = 37.1$ MeV(Fig. 2(b)), however, the whole results have good agreements contrary to the case of $E_{c.m.} = 29.6$ MeV. In the elastic scattering in Fig. 1, elastic cross sections at $E_{c.m.} = 37.1$ MeV have been underestimated, but those for quasi-elastic scattering show much better results rather than those for elastic scattering.

B. Inelastic cross sections

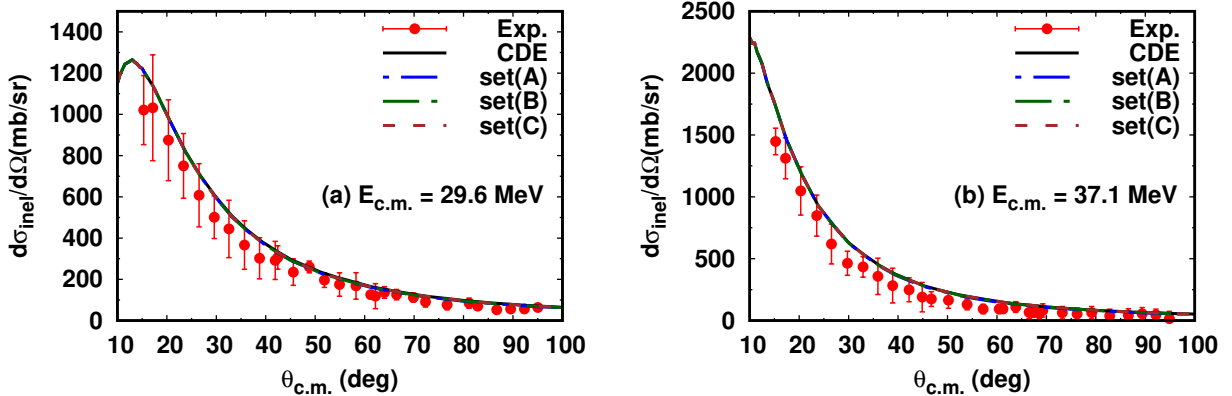


FIG. 3. (Color online) Inelastic scattering cross sections of $^{11}\text{Be} + ^{197}\text{Au}$ system at $E_{c.m.}=29.6$ MeV(a) and $E_{c.m.}=37.1$ MeV (b). The data are taken from Ref. [22].

In Fig. 3, we present results of angular distribution of inelastic scattering using the CDE potential introduced in Eq. (7). For the angular distribution, we use Eqs. (11) and (13). We take the first excitation of ^{11}Be , $\varepsilon_x^{1st} = 0.32$ MeV, with Coulomb dipole strength $B(E1; \varepsilon_x^{1st}) = 0.115 e^2\text{fm}^2$ [30]. Because the neutron separation energy of ^{11}Be is 0.501 MeV, the projectile is broken up for the incident energy considered here. The target excitation in inelastic scattering is also possible. But, we ignore the target excitation because the target excitation states below one neutron separation energy of ^{11}Be are almost E2 and E2+M1, whose energy and contribution are lower than E1. Therefore, we can consider that most of inelastic contributions come from the projectile excitation.

In Fig. 3, cross sections are determined without free parameters after fixing conditions, such as excitation state energies and dipole strengths. Already, we have calculated inelastic cross section for $^{11}\text{Be} + ^{197}\text{Au}$ system in the same manner, which has shown good agreement with experimental data in Ref. [8]. Both results at $E_{c.m.} = 29.6$ MeV and $E_{c.m.} = 37.1$ MeV also show reasonable agreement with experimental data without free parameters. These results are employed for the results of QE scattering presented in Fig. 2 by adding the elastic scattering results in Fig. 1.

Here, we cannot distinguish any differences the results between the results with and without LRN potential. Although partial wave function, $\chi_l^{(+)}(r)$, is influenced by the real part in LRN potential, real parts for LRN potential are very small compared to those for

the bare potential V_{sh} as presented in Table. II. Therefore, in Fig. 3, all inelastic scattering results show almost same results independently of the LRN potential type.

C. Breakup cross sections

In Fig. 4, we present results of breakup cross sections as a function of c.m. angle using the CDE potential in Eq. (8) with and without LRN potential.

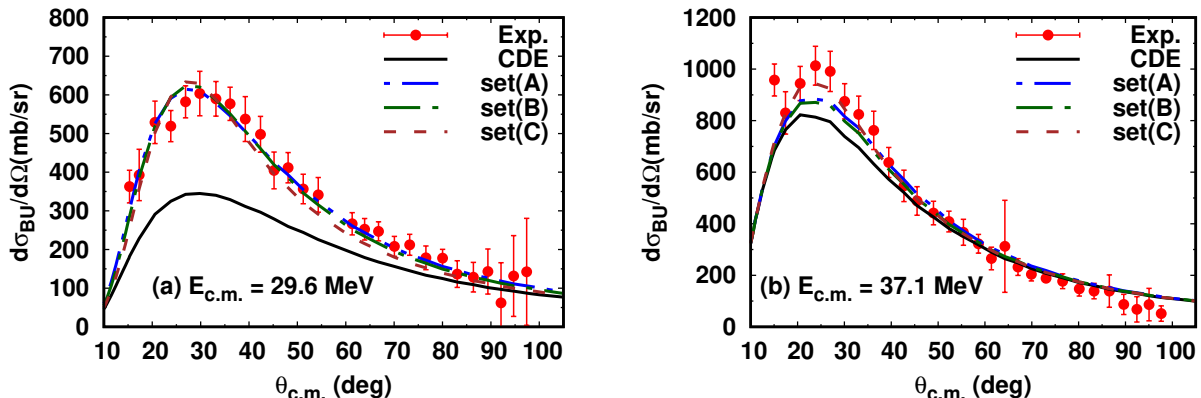


FIG. 4. (Color online) The measured breakup cross section of $^{11}\text{Be} + ^{197}\text{Au}$ system at $E_{\text{c.m.}} = 29.6$ MeV(a) and $E_{\text{c.m.}} = 37.1$ MeV (b). The experimental data are taken from Ref. [22]. The CDE means cross sections only with the CDE potential.

In Fig. 4, the effect of LRN potential, which is not seen in elastic scattering and quasi-elastic scattering cross sections, clearly appeared in the breakup reaction one. In Fig. 4(a), the breakup cross sections are calculated at $E_{\text{c.m.}} = 29.6$ MeV which is slightly below Coulomb barrier. One can easily notice that the results including only CDE potential without LRN potential in (black) solid line definitely underestimated experimental data. It means that CDE potential for breakup reaction including B(E1) distribution is not sufficient to describe experimental data in this energy region. As a result, we need additional LRN potential in Eq.(4). Note that results by the all parameter sets of LRN potential in Table II obtained from the simultaneous χ^2 analysis show good agreement with experimental data. The differences between the sets, (A), (B) and (C) are almost negligible for the case at $E_{\text{c.m.}} = 29.6$ MeV.

In Fig. 4(b), we show the results at $E_{\text{c.m.}} = 37.1$ MeV, which are around Coulomb barrier. Cross sections including only CDE effect without LRN potential in (black) solid line are larger than the case of $E_{\text{c.m.}} = 29.6$ MeV. However, they still underestimated experimental

data. It means that one needs the additional interaction like LRN potential. In this case, we could find the difference of the breakup cross section calculated by parameter sets, (A), (B) and (C). The set (C) in (brown) dashed line is closest to the experimental data. We note that set (C) is the parameter set with longest radius $r_0^{\text{lo}} = r_W^{\text{lo}} = 3.5\text{fm}$ in our scheme. It implies that we have to consider long-range interaction potential in order to describe experimental data relevant to the system including halo nuclei. However, one can not definitely determine the absolute radius of halo nuclei because this radius is a relative scattering length.

Results by the two sets, (A) and (B), denoted as dot-dashed (blue) and dashed-dot (green) line, have almost equal cross sections, and underestimated experimental data although elastic and inelastic cross section data are well explained. Also, in Table II, we notice that diffuseness parameter $a_0^{\text{lo}} = a_W^{\text{lo}}$ decreases by increasing radius because they are intertwined. But they are still huge as 6.24 at $E_{\text{c.m.}} = 29.6\text{ MeV}$.

D. Energy dependency of CDE potential

In Fig. 4, we have presented the contribution of CDE potential for each incident energy, as shown with (black) solid lines of both at (a) $E_{\text{c.m.}} = 29.6\text{ MeV}$ and (b) $E_{\text{c.m.}} = 37.1\text{ MeV}$. In this calculation, we also calculated the breakup cross section only with CDE potential by switching off the LRN potential. Note that we could see that the contribution by the CDE potential increases with the increase of the incident energy, $E_{\text{c.m.}}$ if we compare the breakup cross sections at $E_{\text{c.m.}} = 29.6\text{ MeV}$ and $E_{\text{c.m.}} = 37.1\text{ MeV}$.

To quantitatively understand the increased CDE potential effect along with the increased incident energy, however, we need to analyze the LRN and CDE effects on incident energy in the same frame *i.e.* with the LRN potential switched on. In Fig. 5, one can notice that experimental and theoretical results for breakup cross section are increased at forward angle by increasing the incident energy. Note that main peaks of breakup cross section at forward angle are caused by the long-range Coulomb interaction *i.e.* CDE potential.

Particularly it is noteworthy that the contribution of the CDE potential increases significantly with the increase of the incident energy. This implies that most of the breakup reaction cross section at the incident energy around and above the Coulomb barrier are due to the effect of the CDE potential.

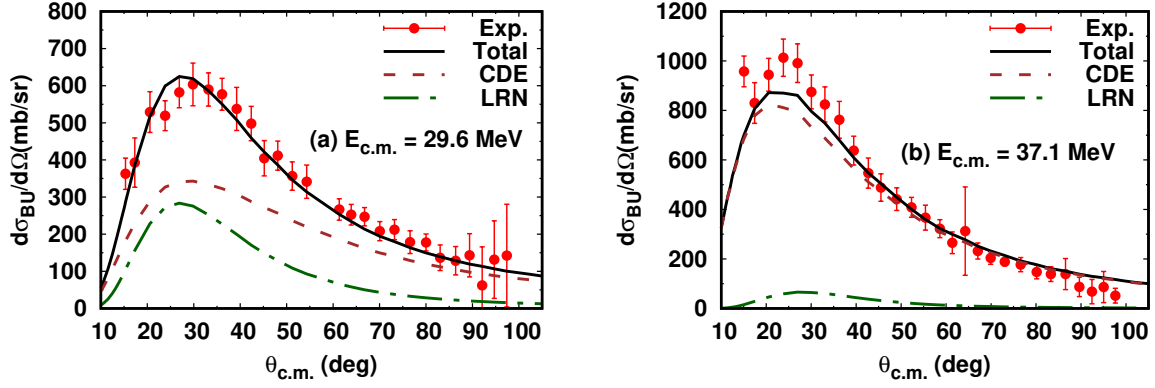


FIG. 5. (Color online) Angular distributions of breakup cross section $d\sigma_{\text{BU}}/d\Omega$ at (a) $E_{\text{c.m.}} = 29.6$ MeV and (b) $E_{\text{c.m.}} = 37.1$ MeV, respectively. Red and blue circles represent the experimental data for $^{11}\text{Be} + ^{197}\text{Au}$ system [22]. The (black) solid, (brown) dashed, and (green) dash-dotted lines show the angular distributions of breakup cross sections with the CDE + LRN (= Total) potential, only with the CDE, and only with LRN, respectively.

E. Necessity of LRN potential

Finally, we argue regarding the necessity of LRN potential depending on the incident energy. As shown in Fig. 5, the CDE potential itself for breakup is not sufficient to describe experimental data at the incident energy below the Coulomb barrier. It means that we have to consider an additional potential like LRN potential at the incident energy below Coulomb barrier. This additional potential is thought to come from complicated interactions. As mentioned in previous sections, the LRN potential which takes implicitly into account the interaction between a valance neutron part of projectile and target nucleus, is caused from halo structure of projectile. Unfortunately, by the limitation of the present optical model, we could not explicitly describe the interaction between a valance neutron part of projectile and target nucleus. However, one can easily notice that they are implicitly taken into account by the contribution of breakup reaction through the imaginary part of the LRN potential in the optical model approach.

Additionally, the present theoretical results in Fig. 5 shows a sharply increasing tendency of the CDE contribution with the increase of the incident energy. If incident energy is sufficiently large, we could conjecture that CDE potential for breakup would cover the LRN

potential effect. Then, there would be no rooms for the LRN potential anymore above certain critical energy point. It means that specific halo properties derived from the effects of the weakly bounded valence neutron(s) would not work anymore, because the LRN potential contributes to describing properties of halo projectile in our description. Therefore, the results in Fig. 5 definitely shows that LRN potential we employed in this calculation plays vital roles of describing scattering experimental data relevant to halo nuclei at the incident energy below Coulomb barrier.

IV. SUMMARY AND CONCLUSIONS

We have simultaneously calculated elastic, quasi-elastic and breakup cross sections of $^{11}\text{Be} + ^{197}\text{Au}$ system, where ^{11}Be has a halo structure, by taking into account long range dynamic polarization potentials, such as Coulomb dipole excitation (CDE) and long range nuclear (LRN) potentials, to the short range nuclear (SRN) potential in an extended optical model (OM) approach. In the present OM scheme, four free parameters in χ^2 analysis have been used for understanding the whole data: elastic, inelastic and breakup cross section data, at 29.6 and 37.1 MeV.

First, we have successfully reproduced recent experimental data for elastic and quasi-elastic scattering around Coulomb barrier, which data were given in terms of the ratio of the elastic and quasi-elastic scattering to Rutherford scattering data. CDE and SRN potentials turned out to be main potentials for properly accounting for most of the elastic and quasi-elastic scattering data. Although the LRN potential contribution was found to be minor, there still remained some rooms for the necessity of LRN potential in the forward scattering region.

Second, therefore, we have studied carefully the energy dependence in the angular distribution data for breakup reaction in order to check the influence of LRN as well as CDE potential. In the low energy region around Coulomb barrier, CDE potential turned out to be insufficient for describing breakup cross sections, specifically, in the forward angle region. This clearly indicates that the scattering data relevant to halo nuclei around Coulomb barrier needs another type's long range potential, *i.e.* LRN potential, stemming from the residual interactions peculiar to halo nuclei scattering in the present OM analysis. But the LRN contribution becomes the smaller with the larger incident energy above Coulomb barrier.

In conclusion, the long range dynamic polarization potentials, such as CDE and LRN potential, are shown to be necessary for properly describing low energy ion scattering by halo nuclei. But, for further definite conclusion for the LRN potential, one needs more experimental data with halo nuclei projectiles especially around Coulomb barrier to be expected from many radioisotope accelerator facilities in near future.

ACKNOWLEDGMENT

This work was supported by the National Research Foundation of Korea (Grant Nos. NRF-2016R1C1B1012874, NRF-2017R1E1A1A01074023, and 2018R1D1A1B07045915).

-
- [1] G. R. Satchler, Direct nuclear reactions, Oxford Univ. press (1983).
 - [2] W. Love, T. Terasawa and G. Satchler, Nuclear Physics A **291**, 183 (1977).
 - [3] W. Y. So, T. Udagawa, K. S. Kim, S. W. Hong and B. T. Kim, Phys. Rev. C **75**, 024610 (2007).
 - [4] W. Y. So, T. Udagawa, S. W. Hong and B. T. Kim, Phys. Rev. C **77**, 024609 (2008).
 - [5] W. Y. So, K. S. Kim, K. S. Choi and M.-K. Cheoun, Phys. Rev. C **90**, 054615 (2014).
 - [6] W. Y. So, K. S. Kim, K. S. Choi and M.-K. Cheoun, Phys. Rev. C **92**, 014627 (2015).
 - [7] W. Y. So, K. S. Kim and M.-K. Cheoun, Phys. Rev. C **89**, 057601 (2014).
 - [8] W. Y. So, K. S. Choi, M.-K. Cheoun and K. S. Kim, Phys. Rev. C **92**, 044618 (2015).
 - [9] W. Y. So, K. S. Choi, M.-K. Cheoun and K. S. Kim, Phys. Rev. C **93**, 054624 (2016).
 - [10] M. Andrés, J. Gómez-Camacho and M. Nagarajan, Nuclear Physics A **579**, 273 (1994).
 - [11] J. Gomez-Camacho, M. Andres and M. Nagarajan, Nuclear Physics A **580**, 156 (1994).
 - [12] M. Andrés, J. Christley, J. Gómez-Camacho and M. Nagarajan, Nuclear Physics A **612**, 82 (1997).
 - [13] I. Tanihata, T. Kobayashi, O. Yamakawa, S. Shimoura, K. Ekuni, K. Sugimoto, N. Takahashi, T. Shimoda and H. Sato, Physics Letters B **206**, 592 (1988).
 - [14] E. F. Aguilera, J. J. Kolata, F. D. Becchetti, P. A. DeYoung, J. D. Hinnefeld, Á. Horváth, L. O. Lamm, H.-Y. Lee, D. Lizcano, E. Martinez-Quiroz, P. Mohr, T. W. O'Donnell, D. A. Roberts and G. Rogachev, Phys. Rev. C **63**, 061603 (2001).

- [15] A. Lemasson, A. Navin, N. Keeley, M. Rejmund, S. Bhattacharyya, A. Shrivastava, D. Bazin, D. Beaumel, Y. Blumenfeld, A. Chatterjee, D. Gupta, G. de France, B. Jacquot, M. Labiche, R. Lemmon, V. Nanal, J. Nyberg, R. G. Pillay, R. Raabe, K. Ramachandran, J. A. Scarpaci, C. Simenel, I. Stefan and C. N. Timis, *Phys. Rev. C* **82**, 044617 (2010).
- [16] J. P. Fernández-García, M. Cubero, M. Rodríguez-Gallardo, L. Acosta, M. Alcorta, M. A. G. Alvarez, M. J. G. Borge, L. Buchmann, C. A. Diget, H. A. Falou, B. R. Fulton, H. O. U. Fynbo, D. Galaviz, J. Gómez-Camacho, R. Kanungo, J. A. Lay, M. Madurga, I. Martel, A. M. Moro, I. Mukha, T. Nilsson, A. M. Sánchez-Benítez, A. Shotter, O. Tengblad and P. Walden, *Phys. Rev. Lett.* **110**, 142701 (2013).
- [17] M. Cubero, J. P. Fernández-García, M. Rodríguez-Gallardo, L. Acosta, M. Alcorta, M. A. G. Alvarez, M. J. G. Borge, L. Buchmann, C. A. Diget, H. A. Falou, B. R. Fulton, H. O. U. Fynbo, D. Galaviz, J. Gómez-Camacho, R. Kanungo, J. A. Lay, M. Madurga, I. Martel, A. M. Moro, I. Mukha, T. Nilsson, A. M. Sánchez-Benítez, A. Shotter, O. Tengblad and P. Walden, *Phys. Rev. Lett.* **109**, 262701 (2012).
- [18] A. M. Vinodkumar, W. Loveland, R. Yanez, M. Leonard, L. Yao, P. Bricault, M. Dombisky, P. Kunz, J. Lassen, A. C. Morton, D. Ottewell, D. Preddy and M. Trinczek, *Phys. Rev. C* **87**, 044603 (2013).
- [19] J. P. Fernández-García, M. Cubero, L. Acosta, M. Alcorta, M. A. G. Alvarez, M. J. G. Borge, L. Buchmann, C. A. Diget, H. A. Falou, B. Fulton, H. O. U. Fynbo, D. Galaviz, J. Gómez-Camacho, R. Kanungo, J. A. Lay, M. Madurga, I. Martel, A. M. Moro, I. Mukha, T. Nilsson, M. Rodríguez-Gallardo, A. M. Sánchez-Benítez, A. Shotter, O. Tengblad and P. Walden, *Phys. Rev. C* **92**, 044608 (2015).
- [20] A. Di Pietro, G. Randisi, V. Scuderi, L. Acosta, F. Amorini, M. J. G. Borge, P. Figuera, M. Fisichella, L. M. Fraile, J. Gomez-Camacho, H. Jeppesen, M. Lattuada, I. Martel, M. Milin, A. Musumarra, M. Papa, M. G. Pellegriti, F. Perez-Bernal, R. Raabe, F. Rizzo, D. Santonocito, G. Scalia, O. Tengblad, D. Torresi, A. M. Vidal, D. Voulot, F. Wenander and M. Zadro, *Phys. Rev. Lett.* **105**, 022701 (2010).
- [21] A. Di Pietro, V. Scuderi, A. M. Moro, L. Acosta, F. Amorini, M. J. G. Borge, P. Figuera, M. Fisichella, L. M. Fraile, J. Gomez-Camacho, H. Jeppesen, M. Lattuada, I. Martel, M. Milin, A. Musumarra, M. Papa, M. G. Pellegriti, F. Perez-Bernal, R. Raabe, G. Randisi, F. Rizzo, G. Scalia, O. Tengblad, D. Torresi, A. M. Vidal, D. Voulot, F. Wenander and M. Zadro, *Phys.*

- Rev. C **85**, 054607 (2012).
- [22] V. Pesudo, M. J. G. Borge, A. M. Moro, J. A. Lay, E. Nácher, J. Gómez-Camacho, O. Tengblad, L. Acosta, M. Alcorta, M. A. G. Alvarez, C. Andreoiu, P. C. Bender, R. Braid, M. Cubero, A. Di Pietro, J. P. Fernández-García, P. Figuera, M. Fisichella, B. R. Fulton, A. B. Garnsworthy, G. Hackman, U. Hager, O. S. Kirsebom, K. Kuhn, M. Lattuada, G. Marquínez-Durán, I. Martel, D. Miller, M. Moukaddam, P. D. O'Malley, A. Perea, M. M. Rajabali, A. M. Sánchez-Benítez, F. Sarazin, V. Scuderi, C. E. Svensson, C. Unsworth and Z. M. Wang, *Phys. Rev. Lett.* **118**, 152502 (2017).
- [23] B. T. Kim, W. Y. So, S. W. Hong and T. Udagawa, *Phys. Rev. C* **65**, 044616 (2002).
- [24] O. Kakuee, J. Rahighi, A. Sánchez-Benítez, M. Andrés, S. Cherubini, T. Davinson, W. Galster, J. Gómez-Camacho, A. Laird, M. Laméhi-Rachti, I. Martel, A. Shotter, W. Smith, J. Vervier and P. Woods, *Nuclear Physics A* **728**, 339 (2003).
- [25] C. Mahaux, H. Ng and G. Satchler, *Nuclear Physics A* **449**, 354 (1986).
- [26] W. Y. So, S. W. Hong, B. T. Kim and T. Udagawa, *Phys. Rev. C* **69**, 064606 (2004).
- [27] J. J. Kolata, E. F. Aguilera, F. D. Becchetti, Y. Chen, P. A. DeYoung, H. García-Martínez, J. D. Hinnefeld, J. H. Lupton, E. Martinez-Quiroz and G. Peaslee, *Phys. Rev. C* **69**, 047601 (2004).
- [28] T. Nakamura, S. Shimoura, T. Kobayashi, T. Teranishi, K. Abe, N. Aoi, Y. Doki, M. Fujimaki, N. Inabe, N. Iwasa, K. Katori, T. Kubo, H. Okuno, T. Suzuki, I. Tanihata, Y. Watanabe, A. Yoshida and M. Ishihara, *Physics Letters B* **331**, 296 (1994).
- [29] G. Borge, J. Maria, V. Pesudo, E. Nácher, A. Perea, A. Moro, J. A. Lay, M. Alvarez, J. P. Fernandez-Garcia, A. Di Prieto and others, *The 26th International Nuclear Physics Conference (proceeding of science)* **281**, 207 (2017).
- [30] F. Ajzenberg-Selove, *Nucl. Phys. A* **506**, 1 (1998).